

Advanced Technique for Assessment of Spatially Averaged Dosimetric Quantities on Nonplanar Surfaces

Ante Kapetanović

Faculty of Electrical Engineering, Mechanical Engineering and Naval Architecture (FESB)

September 25, 2023



Jury Members
President: Prof. Zoran Blažević, PhD

Examiners:	Prof. Zvonimir Šipuš, PhD Assoc. Prof. Kun Li, PhD Assoc. Prof. Vicko Dorić, PhD Assoc. Prof. Mario Cvetković, PhD	Supervisor:	Prof. Dragan Poljak, PhD
------------	---	-------------	--------------------------

Table of contents

1. Introduction

Problem and subject of scientific research

Overview of the existing research

Motivation, purpose and objectives of the research

Hypotheses

2. Materials and methods

Nonplanar models

Estimation of normals

Power density computation and averaging

“Hot-spot” detection

3. Application of research results

Kapetanović and Poljak, *IEEE Trans Electromagn Compat*, 2022.

Kapetanović and Poljak, *Radiat Prot Dosim*, 2023.

Kapetanović et al., *IEEE J Electromagn RF Microw Med Biol*, 2023.

Cvetković et al., *J Commun Softw Syst*, 2022.

4. Concluding remarks

Table of contents

- 1. Introduction**
- 2. Materials and methods**
- 3. Application of research results**
- 4. Concluding remarks**

Problem and subject of scientific research

- The rise in the number of data-intensive wireless devices → expansion of the utilized radio frequency (RF) spectrum into millimeter waves (MMW)¹
- Global roll-out of the fifth-generation (5G) standard for broadband cellular networks → improved communication performance by increasing channel capacity and reducing network latency through²
 - carrier aggregation,
 - multiple-input multiple-output (MIMO) technology,
 - beam-forming, i.e., the spatial filtering,
 - utilization of frequency range (FR) 1 (0.45–6 GHz), FR 2 (24.25–52.6 GHz)
- Increased public interest in (and concerns about) the potential adverse health effects from exposure to RF electromagnetic (EM) radiation³

¹Rappaport et al. 2013.

²Andrews et al. 2014.

³Wu, Rappaport, and Collins 2015.

But what is EM radiation?

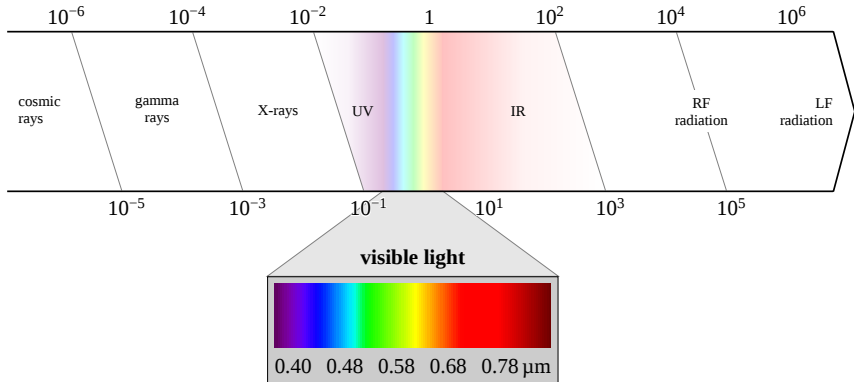


Diagram of the EM spectrum as a function of the wavelength. *Ionizing* radiation occurs when a photon's energy is greater than 10 eV, i.e., under the lower end of ultraviolet (UV) spectrum. Visible, infrared (IR), RF and low-frequency (LF) radiation is thus *non-ionizing*.

Non-ionizing EM radiation effects on biological tissue

⁴International Commission on Non-Ionizing Radiation Protection (ICNIRP) 2020b.

⁵World Health Organization (WHO) n.d.

⁶Ziskin et al., 2018.

Exposure limits to artificial EM fields

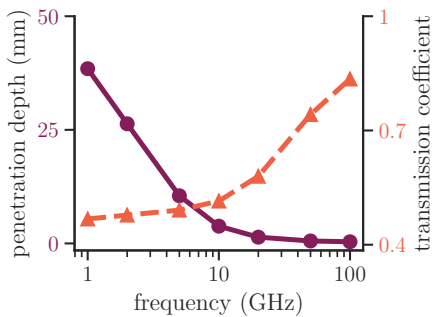
- Prescribed by international guidelines⁷ and standards⁸
- Offer a protection against the possibility of occurrence of adverse health effects by
 - identifying established mechanism of biological interaction,
 - setting allowable limits of exposure,
 - applying safety factors in a conservative manner to account uncertainty
- Derived threshold values → *basic restrictions* or (BR) → *reference levels* (RL)
 - whole-body or local exposure
 - brief or steady-state exposure
- *Specific absorption rate* (SAR) was used as the BR for the steady-state core (whole-body average) and local (10-g or 1-g average) temperature rise from 100 kHz to 300 GHz

⁷International Commission on Non-Ionizing Radiation Protection (ICNIRP) 2020a.

⁸IEEE International Committee on Electromagnetic Safety (ICES) Technical Committee (TC) 95 2019.

Exposure assessment and dosimetry in the era of 5G

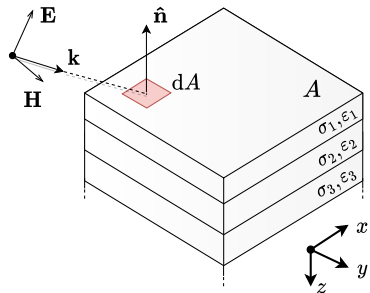
- At 6 GHz, 90 % of the power is absorbed within the uppermost layer of the exposed tissue
- BR are set in terms of the area-averaged *absorbed power density* (APD)
- Line integral of SAR depth-wise into the tissue → *transmitted power density* (TPD)
- Area-averaged TPD ≡ area-averaged APD → consistency and continuity with volume-averaged SAR



Penetration depth and transmission coefficient as a function of frequency

Exposure assessment and dosimetry in the era of 5G

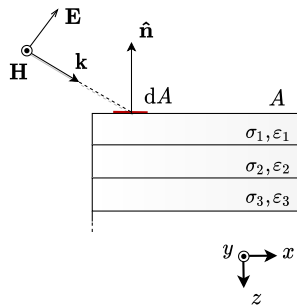
- At 6 GHz, 90 % of the power is absorbed within the uppermost layer of the exposed tissue
- BR are set in terms of the area-averaged *absorbed power density* (APD)
- Line integral of SAR depth-wise into the tissue → *transmitted power density* (TPD)
- Area-averaged TPD ≡ area-averaged APD → consistency and continuity with volume-averaged SAR



Evaluation surface on a multiple-layer tissue-equivalent block model

Exposure assessment and dosimetry in the era of 5G

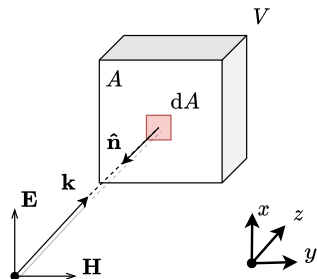
- At 6 GHz, 90 % of the power is absorbed within the uppermost layer of the exposed tissue
- BR are set in terms of the area-averaged *absorbed power density* (APD)
- Line integral of SAR depth-wise into the tissue → *transmitted power density* (TPD)
- Area-averaged TPD ≡ area-averaged APD → consistency and continuity with volume-averaged SAR



Orthographic projection of the evaluation surface on a multiple-layer tissue-equivalent block model

Exposure assessment and dosimetry in the era of 5G

- At 6 GHz, 90 % of the power is absorbed within the uppermost layer of the exposed tissue
- BR are set in terms of the area-averaged *absorbed power density* (APD)
- Line integral of SAR depth-wise into the tissue → *transmitted power density* (TPD)
- Area-averaged TPD ≡ area-averaged APD → consistency and continuity with volume-averaged SAR



A 10-g cubic volume for assessment of SAR during local steady-state exposure below 6 GHz

Governing equations at gigahertz range – APD

- Recent versions of IEEE/ICES-2019 standard and ICNIRP-2020 guidelines propose two distinct definitions of APD
 - 1 spatially averaged normal component of the time-averaged Poynting vector,
 - 2 volume-averaged power loss

$$S_{ab, s} = \frac{1}{2A} \iint_A \Re [\mathbf{E} \times \mathbf{H}^*] \cdot \mathbf{n} \, dA$$

- \mathbf{E}, \mathbf{H} – peak values of the complex phasor electric and magnetic field on the surface
- A – frequency-dependent averaging area
- \mathbf{n} – surface normal on A
- dA – integral area element

Governing equations at gigahertz range – APD

- Recent versions of IEEE/ICES-2019 standard and ICNIRP-2020 guidelines propose two distinct definitions of APD

- ① spatially averaged normal component of the time-averaged Poynting vector,
- ② volume-averaged power loss

$$S_{ab, v} = \frac{1}{A} \iint_A \int_z \rho \text{ SAR} \, dz \, dA$$

$$\text{SAR} = \frac{\sigma |E|^2}{2\rho}$$

- **E** – the peak value of the complex phasor electric field within tissue
- σ – conductivity of tissue
- ρ – tissue density

Governing equation at gigahertz range – IPD

- IPD is the modulus of the time-averaged free-space Poynting vector

$$S_{\text{inc}} = |\mathbf{E} \times \mathbf{H}^*|$$

- Various definitions of the spatially averaged IPD have been proposed and discussed⁹ with the following two standing out in particular

- ➊ spatially averaged normal component of the time-averaged Poynting vector

$$S_{\text{inc, n}} = \frac{1}{2A} \iint_A \Re[\mathbf{E} \times \mathbf{H}^*] \cdot \mathbf{n} \, dA$$

- ➋ spatially averaged magnitude of the time-averaged Poynting vector

$$S_{\text{inc, tot}} = \frac{1}{2A} \iint_A |\mathbf{E} \times \mathbf{H}^*| \, dA$$

- Both definitions correlate well with temperature rise ($r > 0.75$)

⁹IEEE International Committee on Electromagnetic Safety (ICES) Technical Committee (TC) 95 2021.

Sizing the averaging area

- 2–6 GHz → peak value of the power density
- ≥ 6 GHz → averaging on 4 cm^2 square evaluation plane¹⁰
- ≥ 30 GHz → averaging on 1 cm^2 square evaluation plane in addition to account for narrow beam formation¹¹
- Power density spatially averaged on 1 cm^2 area should not exceed twice the value of the 4 cm^2 area¹²

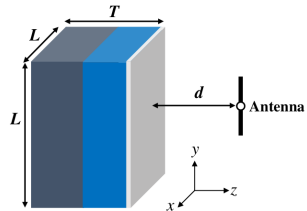
¹⁰Funahashi, Ito, et al. 2018; Hashimoto et al. 2017.

¹¹Foster, Ziskin, and Balzano 2016.

¹²International Commission on Non-Ionizing Radiation Protection (ICNIRP) 2020a.

Tissue models and evaluation surfaces

- Above 6 GHz, flat tissue-equivalent single- or three/four-layer models commonly utilized¹³
 - *stratum corneum*,
 - viable epidermis and dermis,
 - hypodermis,
 - muscle
- Dielectric properties ← four-term Cole-Cole model¹⁴
- Averaging area construction on a planar evaluation surface → IEC/IEEE 63195-2:2022 standard



Skin models with different tissue compositions and the exposure condition. Taken from the recent international inter-comparison study by Li et al. 2021.

¹³Zhadobov et al. 2011.

¹⁴Gabriel 1996.

Current state of the research: A short synthesis

- Definition of the appropriate exposure metric at the 1–10 GHz range¹⁵
- Harmonization of the transition frequency for BRs between existing exposure limits¹⁶
- 10- and 1-g averaging volume → 4 and 1 cm² evaluation plane¹⁷
- First mention of the spatially averaged TPD on the skin surface as a metric to estimate surface temperature rise 6 GHz¹⁸
- Validity of the spatially averaged IPD¹⁹ as RL by various experimental/numerical techniques
- Validity of the spatially averaged APD²⁰ as BR by using the heating factor²¹

¹⁵Anderson, Croft, and McIntosh 2010; McIntosh and Anderson 2010.

¹⁶Colombi, B. Thors, and Törnevik 2015; Björn Thors et al. 2016; Xu et al. 2017.

¹⁷Foster, Ziskin, and Balzano 2016, 2017; Funahashi, Ito, et al. 2018; Hashimoto et al. 2017.

¹⁸Funahashi, Hirata, et al. 2018.

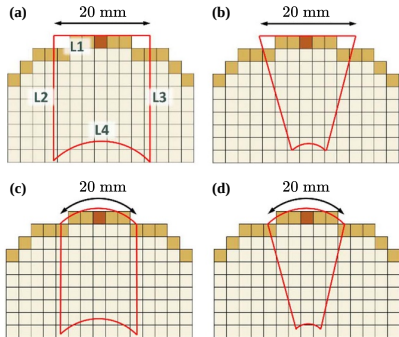
¹⁹Carrasco et al. 2019; De Santis et al. 2022; Diao, K. Li, et al. 2021; He et al. 2018; K. Li, Sasaki, Watanabe, et al. 2019; Miura et al. 2021; Morimoto and Hirata 2022; Nakae et al. 2020; Sasaki et al. 2017.

²⁰K. Li, Kodera, et al. 2023; K. Li, Sasaki, Wake, et al. 2021; Taguchi et al. 2022.

²¹Foster, Ziskin, Balzano, and Bit-Babik 2018.

Current state of the research: Beyond the state of the art

- Nonplanar body parts (fingers²² or ears²³) with the curvature radius \sim wavelength of the incident EM field
→ underestimation of the spatially averaged quantities
- Appropriate curved models currently discussed within a working group under IEEE-ICES TC95 SC6
 - canonical shapes, e.g., sphere²⁴ or cylinder²⁵
 - anatomical tissue models²⁶



Reference averaging volumes for different APD computation schemes in Diao, Rashed and Hirata 2020.

²²C.-H. Li et al. 2012.

²³Sacco, Haider, and Zhadobov 2022.

²⁴Kapetanović and Poljak 2022; Kushiyama and Nagaoka 2022.

²⁵Diao, Rashed, and Hirata 2020; Kapetanović and Poljak 2023.

²⁶Kapetanović, Sacco, et al. 2023.

Motivation, purpose and objectives of the research

- To conduct a *comprehensive investigation into the influence of geometric features and surface morphology of tissue* on the value of APD and IPD above 6 GHz
- To develop an *accurate numerical solver* for surface integrals of the power flow, regardless of underlying numerical/analytical techniques employed in EM simulations
- To develop a *computationally efficient automated detection of the worst-case exposure scenario*—the “hot-spot” region—on the exposed tissue surface

Hypotheses

- ① Traditional flat surfaces for the spatial averaging of power densities are inadequate for RF EM fields with wavelengths comparable to the approximate curvature radius of a nonplanar body part being exposed

Assumption 1

Cylindrical or spherical models are superior for practical compliance assessment of exposure of common nonplanar body parts, e.g., fingers, outer ear, head, ...

Assumption 2

Distribution of surface normal vectors affects the absorption of incident EM fields significantly

Assumption 3

Hybridization of machine learning and traditional numerical methods enhances dosimetry analysis and enables the identification of worst-case exposure scenario without any priors

Hypotheses

- ② Anatomical models with irregularities and asymmetries characterized by intricate convex-concave tissue structures on the surface require high-fidelity numerical estimation of surface normal vectors

Assumption 1

Cylindrical or spherical models are superior for practical compliance assessment of exposure of common nonplanar body parts, e.g., fingers, outer ear, head, ...

Assumption 2

Distribution of surface normal vectors affects the absorption of incident EM fields significantly

Assumption 3

Hybridization of machine learning and traditional numerical methods enhances dosimetry analysis and enables the identification of worst-case exposure scenario without any priors

Hypotheses

- ③ Heterogeneous EM absorption in the near field require evaluating the spatially averaged power density over the entire outer surface of a nonplanar body part being exposed

Assumption 1

Cylindrical or spherical models are superior for practical compliance assessment of exposure of common nonplanar body parts, e.g., fingers, outer ear, head, ...

Assumption 2

Distribution of surface normal vectors affects the absorption of incident EM fields significantly

Assumption 3

Hybridization of machine learning and traditional numerical methods enhances dosimetry analysis and enables the identification of worst-case exposure scenario without any priors

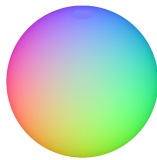
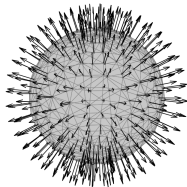
Table of contents

1. Introduction
2. Materials and methods
3. Application of research results
4. Concluding remarks

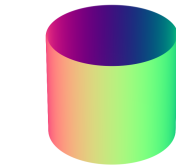
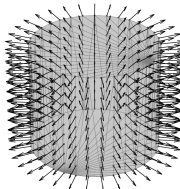
Overview of the methodology

- Development of the appropriate averaging method on curved, canonical surface (IEEE-ICES TC95 SC6 working group on power-density averaging)
- Spatial averaging on anatomical models – highly dependent on the underlying numerical method and the software used during EM simulations
- Estimation of surface normals – crucial for accurate assessment of the surface integrals representing the spatially averaged IPD/APD
- Effective construction of the averaging area and the spatial averaging of the surface-normal propagation-direction power density into the evaluation surface
- Fast and plausible algorithm to extract the “hot-spot” region which yields the peak spatial-average power density

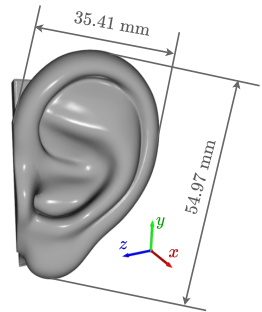
Overview of nonplanar models



Spherical model of the human head²⁷ with radius set to 5 cm



Cylindrical model of the human head²⁸ with radius set to 5 cm



Human ear model²⁹ from Kapetanovic, Sacco et al. 2022.

²⁷Kapetanović and Poljak 2022.

²⁸Kapetanović and Poljak 2023.

²⁹Kapetanović, Sacco, et al. 2023.

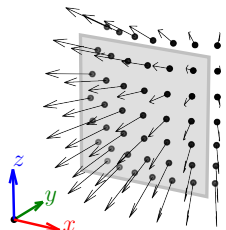
Estimation of normals on canonical surfaces

- Cartesian $(x, y, z) \rightarrow$ ISO 80000-2:2019 spherical (r, θ, φ) coordinate system
 - r – radial distance, i.e., the distance to origin
 - θ – polar angle
 - φ – angle of rotation from the initial meridian plane, i.e., azimuth angle
- Parametric representation of the spherical surface assuming constant r

$$\mathbf{v}(\theta, \varphi) = [r \sin(\theta) \cos(\varphi), r \sin(\theta) \sin(\varphi), r \cos(\theta)]$$

- surface normal vector to the parametric surface

$$\mathbf{n} = -\frac{\mathbf{v}_\theta \times \mathbf{v}_\varphi}{|\mathbf{v}_\theta \times \mathbf{v}_\varphi|}$$



Spherical averaging area (quiver plot) relative to the flat evaluation surface (gray plane)

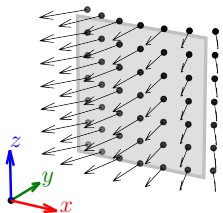
Estimation of normals on canonical surfaces

- Cartesian $(x, y, z) \rightarrow$ ISO 80000-2:2019 cylindrical (r, θ, z) coordinate system
 - r – radial distance, i.e., the distance to origin
 - φ – angle of rotation from the initial meridian plane, i.e., azimuth angle
 - z – axial coordinate
- Parametric representation of the cylindrical surface assuming constant r

$$\mathbf{v}(\varphi, z) = [r \cos(\varphi), r \sin(\varphi), z]$$

- surface normal vector to the parametric surface

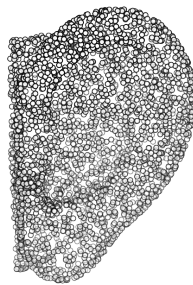
$$\mathbf{n} = -\frac{\mathbf{v}_\theta \times \mathbf{v}_\varphi}{|\mathbf{v}_\theta \times \mathbf{v}_\varphi|}$$



Cylindrical averaging area (quiver plot) relative to the flat evaluation surface (gray plane)

Estimation of normals on anatomically correct models

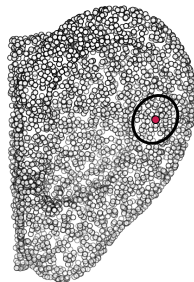
- Assign a normal vector, \mathbf{n} , at each point, \mathbf{x}_i of the point cloud,
$$\mathbb{X} = \{\mathbf{x}_1, \mathbf{x}_2, \dots, \mathbf{x}_n\} \subset \mathbb{R}^3$$
- Organize \mathbb{X} into k-d tree and extract k nearest neighbors of \mathbf{x}_i , $nbhd(\mathbf{x}_i)$
- Create the scatter matrix and compute its principal components
- The eigenvector with the smallest corresponding eigenvalue is orthogonal to the tangent plane $\rightarrow \mathbf{n}$
- Eigenvectors with greater eigenvalues indicate greater variance \rightarrow unit binormal, \mathbf{b} , and tangent vector, \mathbf{t}
- Repeat this for each \mathbf{x}_i in \mathbb{X}



Point cloud of the anatomical tissue model

Estimation of normals on anatomically correct models

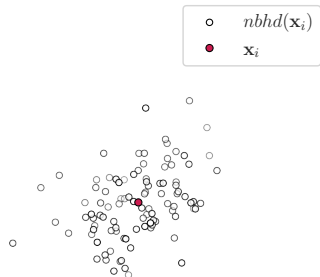
- Assign a normal vector, \mathbf{n} , at each point, \mathbf{x}_i of the point cloud,
 $\mathbb{X} = \{\mathbf{x}_1, \mathbf{x}_2, \dots, \mathbf{x}_n\} \subset \mathbb{R}^3$
- Organize \mathbb{X} into k-d tree and extract k nearest neighbors of \mathbf{x}_i , $nbhd(\mathbf{x}_i)$
- Create the scatter matrix and compute its principal components
- The eigenvector with the smallest corresponding eigenvalue is orthogonal to the tangent plane $\rightarrow \mathbf{n}$
- Eigenvectors with greater eigenvalues indicate greater variance \rightarrow unit binormal, \mathbf{b} , and tangent vector, \mathbf{t}
- Repeat this for each \mathbf{x}_i in \mathbb{X}



Target point \mathbf{x}_i in its local neighborhood defined with a fixed number of neighboring points or within a predefined distance

Estimation of normals on anatomically correct models

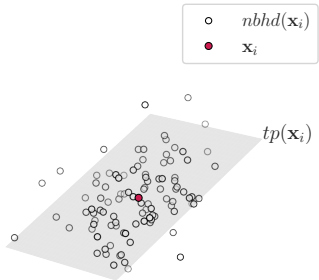
- Assign a normal vector, \mathbf{n} , at each point, \mathbf{x}_i of the point cloud,
$$\mathbb{X} = \{\mathbf{x}_1, \mathbf{x}_2, \dots, \mathbf{x}_n\} \subset \mathbb{R}^3$$
- Organize \mathbb{X} into k-d tree and extract k nearest neighbors of \mathbf{x}_i , $nbhd(\mathbf{x}_i)$
- Create the scatter matrix and compute its principal components
- The eigenvector with the smallest corresponding eigenvalue is orthogonal to the tangent plane $\rightarrow \mathbf{n}$
- Eigenvectors with greater eigenvalues indicate greater variance \rightarrow unit binormal, \mathbf{b} , and tangent vector, \mathbf{t}
- Repeat this for each \mathbf{x}_i in \mathbb{X}



Local patch of points used for fitting the tangent plane

Estimation of normals on anatomically correct models

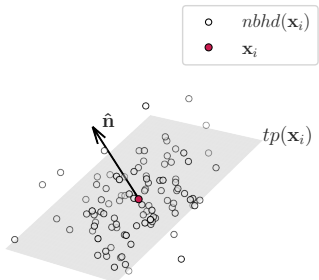
- Assign a normal vector, \mathbf{n} , at each point, \mathbf{x}_i of the point cloud,
$$\mathbb{X} = \{\mathbf{x}_1, \mathbf{x}_2, \dots, \mathbf{x}_n\} \subset \mathbb{R}^3$$
- Organize \mathbb{X} into k-d tree and extract k nearest neighbors of \mathbf{x}_i , $nbhd(\mathbf{x}_i)$
- Create the scatter matrix and compute its principal components
- The eigenvector with the smallest corresponding eigenvalue is orthogonal to the tangent plane $\rightarrow \mathbf{n}$
- Eigenvectors with greater eigenvalues indicate greater variance \rightarrow unit binormal, \mathbf{b} , and tangent vector, \mathbf{t}
- Repeat this for each \mathbf{x}_i in \mathbb{X}



The best fitting tangent plane

Estimation of normals on anatomically correct models

- Assign a normal vector, \mathbf{n} , at each point, \mathbf{x}_i of the point cloud,
$$\mathbb{X} = \{\mathbf{x}_1, \mathbf{x}_2, \dots, \mathbf{x}_n\} \subset \mathbb{R}^3$$
- Organize \mathbb{X} into k-d tree and extract k nearest neighbors of \mathbf{x}_i , $nhd(\mathbf{x}_i)$
- Create the scatter matrix and compute its principal components
- The eigenvector with the smallest corresponding eigenvalue is orthogonal to the tangent plane $\rightarrow \mathbf{n}$
- Eigenvectors with greater eigenvalues indicate greater variance \rightarrow unit binormal, \mathbf{b} , and tangent vector, \mathbf{t}
- Repeat this for each \mathbf{x}_i in \mathbb{X}

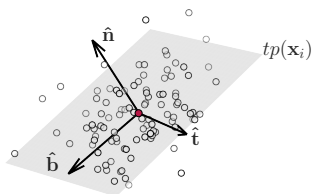


The unit normal vector in \mathbf{x}_i is orthogonal to the local tangent plane

Estimation of normals on anatomically correct models

- Assign a normal vector, \mathbf{n} , at each point, \mathbf{x}_i of the point cloud,
$$\mathbb{X} = \{\mathbf{x}_1, \mathbf{x}_2, \dots, \mathbf{x}_n\} \subset \mathbb{R}^3$$
- Organize \mathbb{X} into k-d tree and extract k nearest neighbors of \mathbf{x}_i , $nbhd(\mathbf{x}_i)$
- Create the scatter matrix and compute its principal components
- The eigenvector with the smallest corresponding eigenvalue is orthogonal to the tangent plane $\rightarrow \mathbf{n}$
- Eigenvectors with greater eigenvalues indicate greater variance \rightarrow unit binormal, \mathbf{b} , and tangent vector, \mathbf{t}
- Repeat this for each \mathbf{x}_i in \mathbb{X}

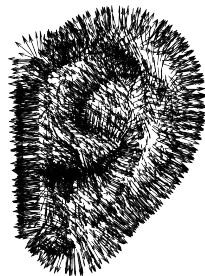
○ $nbhd(\mathbf{x}_i)$
● \mathbf{x}_i



The unit binormal and tangent vector in orthonormal basis

Estimation of normals on anatomically correct models

- Assign a normal vector, \mathbf{n} , at each point, \mathbf{x}_i of the point cloud,
$$\mathbb{X} = \{\mathbf{x}_1, \mathbf{x}_2, \dots, \mathbf{x}_n\} \subset \mathbb{R}^3$$
- Organize \mathbb{X} into k-d tree and extract k nearest neighbors of \mathbf{x}_i , $nbhd(\mathbf{x}_i)$
- Create the scatter matrix and compute its principal components
- The eigenvector with the smallest corresponding eigenvalue is orthogonal to the tangent plane $\rightarrow \mathbf{n}$
- Eigenvectors with greater eigenvalues indicate greater variance \rightarrow unit binormal, \mathbf{b} , and tangent vector, \mathbf{t}
- Repeat this for each \mathbf{x}_i in \mathbb{X}



Distribution of the unit vector field normal to the surface

Local tangent plane fitting

- $nghd(\mathbf{x}_i)$ is represented by the “centroid”

$$\mathbf{m}_i = \frac{1}{k} \sum_{j=1}^k \mathbf{x}_j$$

where $\mathbf{x}_j \in nhd(\mathbf{x}_i)$

- The tangential plane is found by minimizing the Euclidian vector distance, \mathbf{y}_j between each point in $nhd(\mathbf{x}_i)$ and \mathbf{m}_i

$$\min_{\|\mathbf{n}_i\|=1} \sum_{j=1}^k (\mathbf{y}_j^\top \mathbf{n}_i)^2$$

- Above expression can be rewritten in a matrix notation as

$$\min_{\mathbf{n}_i^\top \mathbf{n}_i = 1} \mathbf{n}_i^\top (\mathbf{Y}_i \mathbf{Y}_i^\top) \mathbf{n}_i$$

where

$$\mathbf{Y}_i = \begin{pmatrix} | & | & & | & & | \\ \mathbf{y}_1 & \mathbf{y}_2 & \dots & \mathbf{y}_j & \dots & \mathbf{y}_k \\ | & | & & | & & | \end{pmatrix}$$

Constrained minimization via Lagrange multipliers

- A function $f(\mathbf{n}_i) = \mathbf{n}_i^\top \mathbf{S}_i \mathbf{n}_i$ where $\mathbf{S}_i = \mathbf{Y}_i \mathbf{Y}_i^\top$ should be minimized s.t. $\mathbf{n}_i^\top \mathbf{n}_i = 1$
- Instead of constrained optimization, $f(\mathbf{n}_i)$ is subjected to the equality constraint $g(\mathbf{n}_i) = \mathbf{n}_i^\top \mathbf{n}_i - 1$ and the Lagrangian function is formed

$$\mathcal{L}(\mathbf{n}_i, \lambda) = f(\mathbf{n}_i) - \lambda g(\mathbf{n}_i)$$

- The constrained minimization of $f(\mathbf{n}_i)$ is now equivalent to the unconstrained minimization of $\mathcal{L}(\mathbf{n}_i, \lambda)$

$$\nabla \mathcal{L}(\mathbf{n}_i, \lambda) = 0$$

$$\frac{\partial \mathcal{L}}{\partial \mathbf{n}_i} = 0 \Rightarrow \mathbf{S}_i \mathbf{n}_i = \lambda \mathbf{n}_i$$

$$\frac{\partial \mathcal{L}}{\partial \lambda} = 0 \Rightarrow \mathbf{n}_i^\top \mathbf{n}_i = 1$$

- The normal is the eigenvector \mathbf{S}_i with the smallest associated λ

$$\mathbf{S}_i = \mathbf{V} \begin{pmatrix} \lambda_1 & & \\ & \ddots & \\ & & \lambda_d \end{pmatrix} \mathbf{V}^\top$$

Assessment of the curvature, i.e., “non-unit” normal vector

- By using the local frame computed at \mathbf{x}_i with the principal component analysis (PCA), $nbhd(\mathbf{x}_i)$ can be represented implicitly as $[u, v, f(u, v)]$
- The parametric surface is expressed in the local frame’s basis, i.e., with the principal component vectors
 - u, v – tangential coordinates
 - $f(u, v)$ – the “height” function in the normal direction
- Instead of a plane, a high-order polynomial³⁰, implicit B-spline³¹, n-jet (truncated Taylor expansion)³², etc. can be fitted to such parametric surface representation
- Curvature normal is then computed as

$$\mathbf{n} = \frac{\partial \tilde{f}}{\partial u} \times \frac{\partial \tilde{f}}{\partial v}$$

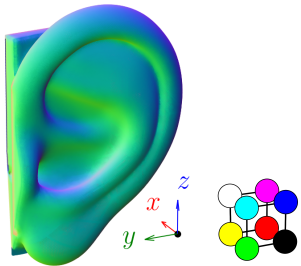
at $u = v = 0$ where $\tilde{f}(u, v)$ is the fitted “height” function

³⁰Levin 1998.

³¹Mohammad Rouhani 2015.

³²Cazals and Pouget 2005.

Surface normal vector estimation via moving least squares



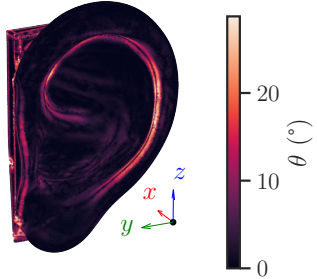
Surface normal vector field distribution estimated by moving least squares (weighted with radial basis function) applied to the parametric surface embedded in the local frame's basis

- Weighted moving least squares generally performs well and is able to capture curvature better compared to the simple plane fitting
- Fails at sharp edges or corners, i.e., non-differentiable and non-smooth regions of the surface
- This can be alleviated by using either regression-based deep learning methods³³ or surface fitting-based deep learning methods (traditional surface fitting methods powered by the learned weights)³⁴

³³Ben-Shabat, Lindenbaum, and Fischer 2019; Charles et al. 2017; Guerrero et al. 2018.

³⁴Ben-Shabat and Gould 2020; Lenssen, Osendorfer, and Masci 2020; Zhu et al. 2021.

Surface normal vector estimation via moving least squares



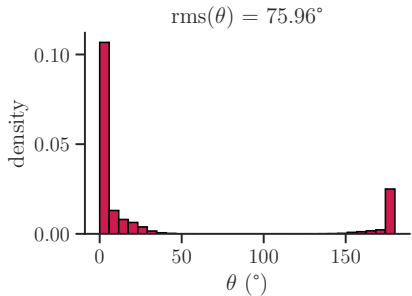
Spatial distribution of angle error between normals computed by using moving least squares and PCA (ground truth, but still prone to instabilities and errors)

- Weighted moving least squares generally performs well and is able to capture curvature better compared to the simple plane fitting
- Fails at sharp edges or corners, i.e., non-differentiable and non-smooth regions of the surface
- This can be alleviated by using either regression-based deep learning methods³³ or surface fitting-based deep learning methods (traditional surface fitting methods powered by the learned weights)³⁴

³³Ben-Shabat, Lindenbaum, and Fischer 2019; Charles et al. 2017; Guerrero et al. 2018.

³⁴Ben-Shabat and Gould 2020; Lenssen, Osendorfer, and Masci 2020; Zhu et al. 2021.

Surface normal vector estimation via moving least squares



Histogram of angle error – difficulty in dealing with non-differentiable regions results in large deviations

- Weighted moving least squares generally performs well and is able to capture curvature better compared to the simple plane fitting
- Fails at sharp edges or corners, i.e., non-differentiable and non-smooth regions of the surface
- This can be alleviated by using either regression-based deep learning methods³³ or surface fitting-based deep learning methods (traditional surface fitting methods powered by the learned weights)³⁴

³³Ben-Shabat, Lindenbaum, and Fischer 2019; Charles et al. 2017; Guerrero et al. 2018.

³⁴Ben-Shabat and Gould 2020; Lenssen, Osendorfer, and Masci 2020; Zhu et al. 2021.

Normal orientation

- The local frame at \mathbf{x}_i contains arbitrarily oriented eigenvectors due to PCA
- Consistent orientation – normals, \mathbf{n}_i and \mathbf{n}_j , of any two neighboring points, \mathbf{x}_i and \mathbf{x}_j , should point in similar direction
- $\mathbf{n}_i \cdot \mathbf{n}_j \approx \pm 1 \rightarrow tp(\mathbf{x}_i)$ and $tp(\mathbf{x}_j)$ are parallel
- $\mathbf{n}_i \cdot \mathbf{n}_j \approx 1 \checkmark$
- If the above condition is not met, \mathbf{n}_i or \mathbf{n}_j should be flipped
- Disadvantages
 - ① fails at sharp edges and corners
 - ② this should hold for *all* pairs of neighboring points in the point cloud

Normal orientation

- The local frame at \mathbf{x}_i contains arbitrarily oriented eigenvectors due to PCA
- Consistent orientation – normals, \mathbf{n}_i and \mathbf{n}_j , of any two neighboring points, \mathbf{x}_i and \mathbf{x}_j , should point in similar direction
- $\mathbf{n}_i \cdot \mathbf{n}_j \approx \pm 1 \rightarrow tp(\mathbf{x}_i)$ and $tp(\mathbf{x}_j)$ are parallel
- $\mathbf{n}_i \cdot \mathbf{n}_j \approx 1 \checkmark$
- If the above condition is not met, \mathbf{n}_i or \mathbf{n}_j should be flipped
- Disadvantages Possible solutions

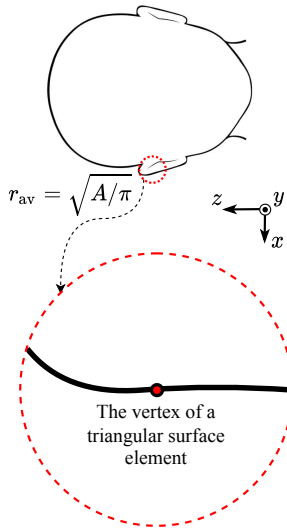
- ① anatomical tissue models do not contain sharp edges and corners; otherwise methods that handle noise, outliers and sharp features available³⁵
- ② posing a problem as graph optimization by
 - constructing a graph over the point cloud
 - assigning a weight to each edge based on the “similarity score”

$$w_{ij} = 1 - |\mathbf{n}_i \cdot \mathbf{n}_j|$$

- constructing a minimal spanning tree
- propagating the normal orientation from a single point selected as the root
- the favorable propagation along directions of low curvature \rightarrow avoiding edges

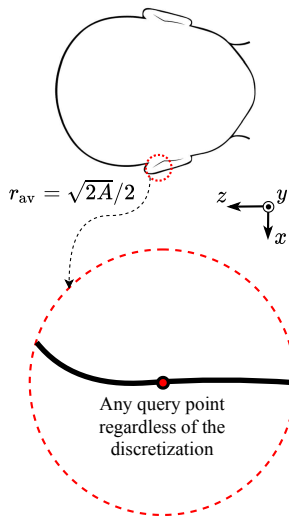
³⁵Huang et al. 2009.

Construction of the conformal averaging area



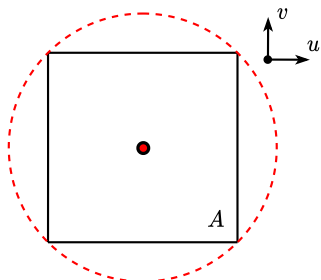
- IEC-IEEE 63195 standard
 - reconstruct surface as triangle mesh (max. edge length up to $\lambda/10$)
 - extract a circular area as the *cross section* between the evaluation surface and sphere with radius $\sqrt{A/\pi}$ placed at a *vertex*
- Our approach considers radius of the circumscribed circle of the square-shaped averaging area instead
- Extracted circular area reduced to a square shape of an area A in orthonormal basis
- The resulting projection is mapped onto the nonplanar evaluation surface

Construction of the conformal averaging area



- IEC-IEEE 63195 standard
 - reconstruct surface as triangle mesh (max. edge length up to $\lambda/10$)
 - extract a circular area as the *cross section* between the evaluation surface and sphere with radius $\sqrt{A/\pi}$ placed at a vertex
- Our approach considers radius of the circumscribed circle of the square-shaped averaging area instead
- Extracted circular area reduced to a square shape of an area A in orthonormal basis
- The resulting projection is mapped onto the nonplanar evaluation surface

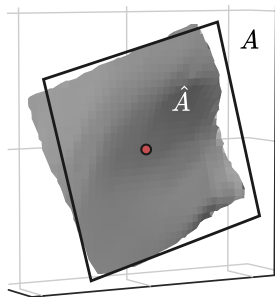
Construction of the conformal averaging area



Projection of the averaging area in orthonormal basis

- IEC-IEEE 63195 standard
 - reconstruct surface as triangle mesh (max. edge length up to $\lambda/10$)
 - extract a circular area as the *cross section* between the evaluation surface and sphere with radius $\sqrt{A/\pi}$ placed at a vertex
- Our approach considers radius of the circumscribed circle of the square-shaped averaging area instead
- Extracted circular area reduced to a square shape of an area A in orthonormal basis
- The resulting projection is mapped onto the nonplanar evaluation surface

Construction of the conformal averaging area



Spatial relationship between the conformal averaging area, \hat{A} , and its projection, A

- IEC-IEEE 63195 standard
 - reconstruct surface as triangle mesh (max. edge length up to $\lambda/10$)
 - extract a circular area as the *cross section* between the evaluation surface and sphere with radius $\sqrt{\hat{A}/\pi}$ placed at a vertex
- Our approach considers radius of the circumscribed circle of the square-shaped averaging area instead
- Extracted circular area reduced to a square shape of an area A in orthonormal basis
- The resulting projection is mapped onto the nonplanar evaluation surface

Practical considerations for the spatial averaging

- The spatially averaged surface-normal propagation-direction power density into the evaluation surface

$$sPD_n(\mathbf{r}_0) = \frac{1}{2\hat{A}(\mathbf{r}_0)} \iint_{A(\mathbf{r}_0)} \Theta \{ \Re [\mathbf{E}(\mathbf{r}) \times \mathbf{H}^*(\mathbf{r})] \cdot \mathbf{n}(\mathbf{r}) \} \cdot \Re [\mathbf{E}(\mathbf{r}) \times \mathbf{H}^*(\mathbf{r})] \cdot \mathbf{n}(\mathbf{r}) d\hat{A}(\mathbf{r})$$

where

- \hat{A} – conformal averaging area
 - \mathbf{r} – positional vector to a point on \hat{A}
 - \mathbf{r}_0 – positional vector to a query point (center of \hat{A})
 - $\Theta(\cdot)$ – the Heaviside function → sets integrand to 0 if $\angle(\mathbf{n}, \mathbf{E} \times \mathbf{H}^*) = [90, 270]^\circ$
- $\hat{A} > A$
 - the more pronounced the curvature, the greater the difference
 - \hat{A} can be estimated directly by integrating the normals

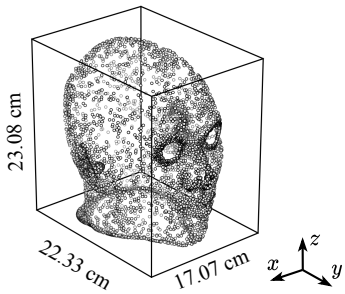
“Hot-spot” detection: Approach

- ① Organize an oriented set of points, $\mathbb{X} = \{\mathbf{x}_1, \mathbf{x}_2, \dots, \mathbf{x}_i, \dots, \mathbf{x}_n\} \subset \mathbb{R}^3$, representing the nonplanar model into a 3D k-d tree³⁶
- ② Identify points visible from the predefined direction³⁷ corresponding to the propagation direction of incident EM fields
- ③ For a point, \mathbf{x}_i , in the visible subset of points, extract $nbhd(\mathbf{x}_i)$ within a sphere of a radius $\sqrt{2A}/2$, where A is the size of the square integration domain
- ④ Perform a change of basis on the local neighborhood using the PCA → alignment of the tangential principal components with A
- ⑤ Extract the area of a conformal averaging area, \hat{A} , by approximating the surface integral of the magnitude of surface normals on the corresponding surface
- ⑥ Compute the spatially averaged power density
- ⑦ Repeat steps 3 to 6 until convergence
- ⑧ Report the peak spatial-average power density → worst-case exposure scenario

³⁶Bentley 1975.

³⁷Katz, Tal, and Basri 2007.

“Hot-spot” detection: Illustrative example



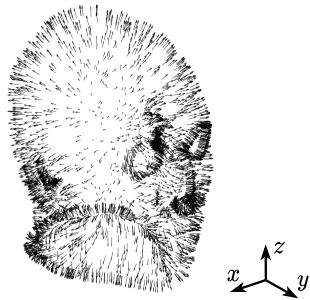
- Realistic human head model represented by 63 333 surface points³⁸
- Surface normal vectors estimated by weighted moving least-squares approach
- Surface reconstructed as a triangle mesh by using the Poisson method³⁹
- Exposure to RF energy absorbed in a distorted Gaussian pattern⁴⁰
- Resulting region of highest exposure

³⁸Laakso et al. 2015.

³⁹Kazhdan, Bolitho, and Hoppe 2006.

⁴⁰Kapetanović, Poljak, and Dodig 2023.

“Hot-spot” detection: Illustrative example



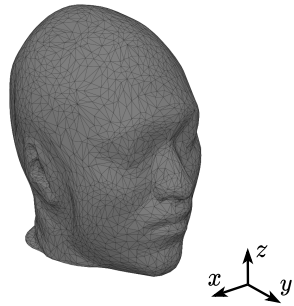
- Realistic human head model represented by 63 333 surface points³⁸
- Surface normal vectors estimated by weighted moving least-squares approach
- Surface reconstructed as a triangle mesh by using the Poisson method³⁹
- Exposure to RF energy absorbed in a distorted Gaussian pattern⁴⁰
- Resulting region of highest exposure

³⁸Laakso et al. 2015.

³⁹Kazhdan, Bolitho, and Hoppe 2006.

⁴⁰Kapetanović, Poljak, and Dodig 2023.

“Hot-spot” detection: Illustrative example



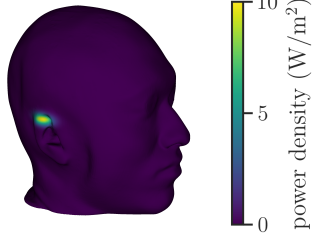
- Realistic human head model represented by 63 333 surface points³⁸
- Surface normal vectors estimated by weighted moving least-squares approach
- Surface reconstructed as a triangle mesh by using the Poisson method³⁹
- Exposure to RF energy absorbed in a distorted Gaussian pattern⁴⁰
- Resulting region of highest exposure

³⁸Laakso et al. 2015.

³⁹Kazhdan, Bolitho, and Hoppe 2006.

⁴⁰Kapetanović, Poljak, and Dodig 2023.

“Hot-spot” detection: Illustrative example



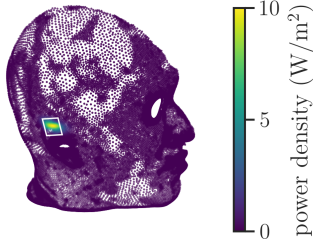
- Realistic human head model represented by 63 333 surface points³⁸
- Surface normal vectors estimated by weighted moving least-squares approach
- Surface reconstructed as a triangle mesh by using the Poisson method³⁹
- **Exposure to RF energy absorbed in a distorted Gaussian pattern⁴⁰**
- Resulting region of highest exposure

³⁸Laakso et al. 2015.

³⁹Kazhdan, Bolitho, and Hoppe 2006.

⁴⁰Kapetanović, Poljak, and Dodig 2023.

“Hot-spot” detection: Illustrative example



- Realistic human head model represented by 63 333 surface points³⁸
- Surface normal vectors estimated by weighted moving least-squares approach
- Surface reconstructed as a triangle mesh by using the Poisson method³⁹
- Exposure to RF energy absorbed in a distorted Gaussian pattern⁴⁰
- **Resulting region of highest exposure**

³⁸Laakso et al. 2015.

³⁹Kazhdan, Bolitho, and Hoppe 2006.

⁴⁰Kapetanović, Poljak, and Dodig 2023.

Table of contents

1. Introduction
2. Materials and methods
3. Application of research results
4. Concluding remarks

Computational results

Overview of the results published in 4 different peer-reviewed papers—the basis of the thesis—is given through the following descriptors

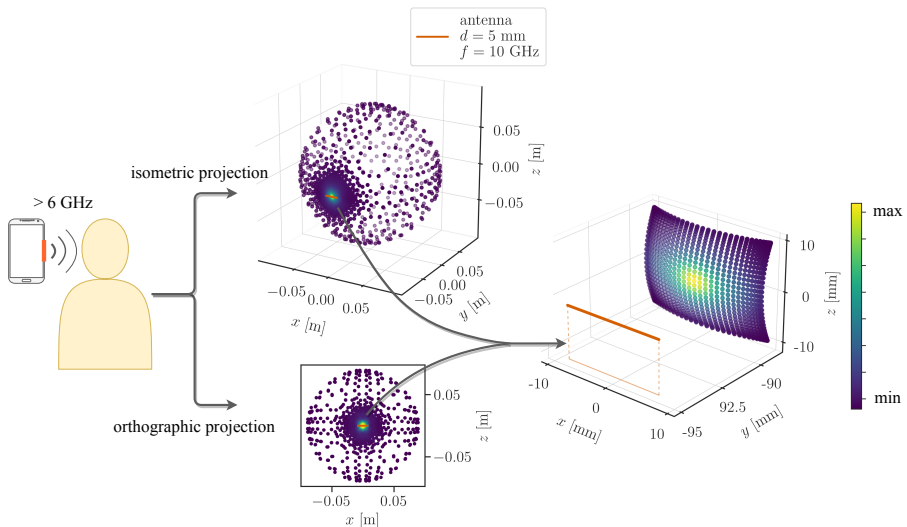
- ① Scope
- ② Model and methods
 - antenna model
 - tissue model
 - exposure scenario
 - numerical methods for EM simulation
 - postprocessing
- ③ Reported result and takeaways

Published paper #1: Scope

Kapetanović, Ante and Poljak, Dragan “Assessment of incident power density on spherical head model up to 100 GHz,” in *IEEE Trans Electromagn Compat*, 64(5):1296–1303, 2022, doi: 10.1109/TEMC.2022.3183071

- Utilization of the spherical model of the human head
- Development of an accurate technique for IPD averaging in spherical coordinates
- Comparison of two existing definitions of the spatially averaged IPD by considering the normal component and magnitude of the Poynting vector
- Comparison of the quantities extracted from the spherical and three distinctly positioned flat evaluation surfaces relative to the spherical one
- Quantification of the effect of the curvature and putting it into the context with current exposure limits

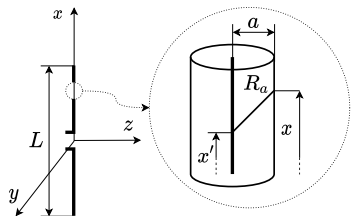
Published paper #1: Model and methods



⁴¹Poljak 2007.

⁴²Kapetanovic and Poljak 2021.

Published paper #1: Model and methods



- A center-fed half-wavelength dipole driven by a 1-V source
- Current distribution, $I(x')$, governed by the Pocklington integro-differential equation → Galerkin-Bubnov indirect boundary element method (GB-IBEM)⁴¹
- Electric-field components obtained at any point on the surface of the tissue → boundary element formalism with automatic differentiation⁴²
- Spherical (shaded gray) and near- (orange square), middle- (blue dashed square) and far-flat (green dot-dashed square) evaluation surfaces

⁴¹Poljak 2007.

⁴²Kapetanovic and Poljak 2021.

Published paper #1: Model and methods

$$E_x^{exc} = j\omega \frac{\mu_0}{4\pi} \int_{-L/2}^{L/2} I(x') g_a \, dx' - \frac{1}{j4\pi\omega\epsilon_0} \frac{\partial}{\partial x} \int_{-L/2}^{L/2} \frac{\partial I(x')}{\partial x'} g_a \, dx'$$

where

$$g_a = g_a(x, x') = \frac{\exp(-jkR_a)}{R_a},$$

$$R_a = |x', x|$$

- A center-fed half-wavelength dipole driven by a 1-V source
- Current distribution, $I(x')$, governed by the Pocklington integro-differential equation → Galerkin-Bubnov indirect boundary element method (GB-IBEM)⁴¹
- Electric-field components obtained at any point on the surface of the tissue → boundary element formalism with automatic differentiation⁴²
- Spherical (shaded gray) and near- (orange square), middle- (blue dashed square) and far-flat (green dot-dashed square) evaluation surfaces

⁴¹Poljak 2007.

⁴²Kapetanovic and Poljak 2021.

Published paper #1: Model and methods

$$E_x = \frac{1}{j4\pi\omega\epsilon_0} \left[\int_{-L/2}^{L/2} \frac{\partial I(x')}{\partial x'} \frac{\partial g}{\partial x} dx' - k^2 \int_{-L/2}^{L/2} I(x') g dx' \right]$$

$$E_y = \frac{1}{j4\pi\omega\epsilon_0} \int_{-L/2}^{L/2} \frac{\partial I(x')}{\partial x'} \frac{\partial g}{\partial y} dx'$$

$$E_z = \frac{1}{j4\pi\omega\epsilon_0} \int_{-L/2}^{L/2} \frac{\partial I(x')}{\partial x'} \frac{\partial g}{\partial z} dx'$$

where

$$g = g(x, y, z, x') = \frac{\exp(-jkR)}{R},$$

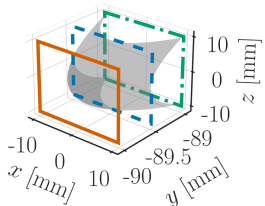
$$R = |(x'), (x, y, z)|$$

- A center-fed half-wavelength dipole driven by a 1-V source
- Current distribution, $I(x')$, governed by the Pocklington integro-differential equation → Galerkin-Bubnov indirect boundary element method (GB-IBEM)⁴¹
- Electric-field components obtained at any point on the surface of the tissue → boundary element formalism with automatic differentiation⁴²
- Spherical (shaded gray) and near- (orange square), middle- (blue dashed square) and far-flat (green dot-dashed square) evaluation surfaces

⁴¹Poljak 2007.

⁴²Kapetanovic and Poljak 2021.

Published paper #1: Model and methods



- A center-fed half-wavelength dipole driven by a 1-V source
- Current distribution, $I(x')$, governed by the Pocklington integro-differential equation → Galerkin-Bubnov indirect boundary element method (GB-IBEM)⁴¹
- Electric-field components obtained at any point on the surface of the tissue → boundary element formalism with automatic differentiation⁴²
- Spherical (shaded gray) and near- (orange square), middle- (blue dashed square) and far-flat (green dot-dashed square) evaluation surfaces

⁴¹Poljak 2007.

⁴²Kapetanovic and Poljak 2021.

Published paper #1: Reported result and takeaways

- Time-averaged Poynting vector representing the direction and density of EM-power flow into the tissue

$$\mathbf{S} = \frac{1}{2} \Re (\mathbf{E} \times \mathbf{H}^*)$$

- Evaluation surface in spherical coordinate system (r, θ, φ) , ISO 80000-2:2019

$$\mathbf{v}(\theta, \varphi) = [r \sin(\theta) \cos(\varphi), r \sin(\theta) \sin(\varphi), r \cos(\theta)]$$

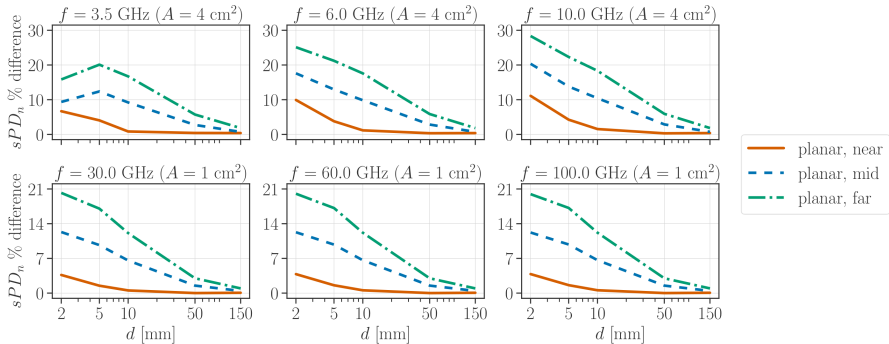
- Definition 1: Normal component \rightarrow spherical coordinate system

$$sPD_n = \frac{1}{A} \iint \mathbf{S}(\mathbf{v}) \cdot (\mathbf{v}_\theta \times \mathbf{v}_\varphi) \, d\theta d\varphi$$

- Definition 2: Norm \rightarrow spherical coordinate system

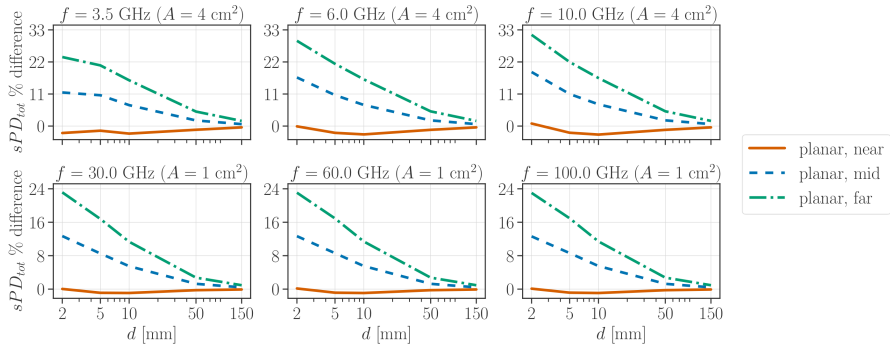
$$sPD_{tot} = \frac{1}{A} \iint |\mathbf{S}(\mathbf{v})| r^2 \sin(\theta) \, d\theta d\varphi$$

Published paper #1: Reported result and takeaways



Relative differences averaged over the near-, middle- and far-flat with a spherical surface as functions of the separation distance from the antenna at 3.5, 6, 10, 30.60 and 100 GHz

Published paper #1: Reported result and takeaways



Relative differences averaged over the near-, middle- and far-flat with a spherical surface as functions of the separation distance from the antenna at 3.5, 6, 10, 30.60 and 100 GHz

Published paper #1: Reported result and takeaways

Absolute percentage differences between sPD_n and sPD_{tot} on a spherical surface at different separation distances from the antenna at 6 and 30 GHz

		d , mm	2	5	10	50	150
6 GHz	sPD_n	8.30	5.54	3.03	0.22	0.03	
	sPD_{tot}	12.16	6.69	3.27	0.22	0.03	
	% difference*	37.79	18.94	7.75	0.16	0.07	
30 GHz	sPD_n	27.18	12.93	4.81	0.23	0.03	
	sPD_{tot}	36.04	14.44	5.01	0.23	0.03	
	% difference*	28.04	11.07	4.02	0.06	0.02	

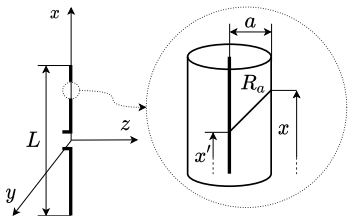
Published paper #2: Scope

Kapetanović, A. and Poljak, D. "Machine learning-assisted antenna modeling for realistic assessment of incident power density on non-planar surfaces above 6 GHz," in *Radiat Prot Dosim*, 199(8–9):826–834, 2023, doi: 10.1093/rpd/ncad114

- Utilization of the cylindrical model of a body part
- Development of an accurate technique for IPD averaging in cylindrical coordinates
- Comparison of the spherical with cylindrical model by using the flat model as a reference
- Capturing the effect of the curvature by varying the curvature radius
- Upgrading EM simulation of exposure by aiding traditional numerical techniques with machine learning → differentiable programming⁴³

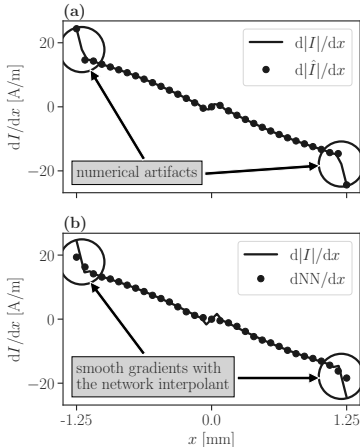
⁴³Innes et al. 2019.

Published paper #2: Model and methods



- A center-fed half-wavelength dipole, the input power normalized to 10 mW
- Current distribution, $I(x')$, governed by the Pocklington integro-differential equation →
(a) GB-IBEM, (b) GB-IBEM + neural network for smooth gradients at critical elements
- Electric-field components obtained at any point on the surface of the tissue → boundary element formalism with automatic differentiation
- Reference flat compared to (a) spherical and
(b) cylindrical evaluation surfaces

Published paper #2: Model and methods



- A center-fed half-wavelength dipole, the input power normalized to 10 mW
- Current distribution, $I(x')$, governed by the Pocklington integro-differentional equation → (a) GB-IBEM, (b) GB-IBEM + neural network for smooth gradients at critical elements
- Electric-field components obtained at any point on the surface of the tissue → boundary element formalism with automatic differentiation
- Reference flat compared to (a) spherical and (b) cylindrical evaluation surfaces

Published paper #2: Model and methods

$$E_x = \frac{1}{j4\pi\omega\epsilon_0} \left[\int_{-L/2}^{L/2} \frac{\partial I(x')}{\partial x'} \frac{\partial g}{\partial x} dx' - k^2 \int_{-L/2}^{L/2} I(x')g dx' \right]$$

$$E_y = \frac{1}{j4\pi\omega\epsilon_0} \int_{-L/2}^{L/2} \frac{\partial I(x')}{\partial x'} \frac{\partial g}{\partial y} dx'$$

$$E_z = \frac{1}{j4\pi\omega\epsilon_0} \int_{-L/2}^{L/2} \frac{\partial I(x')}{\partial x'} \frac{\partial g}{\partial z} dx'$$

where

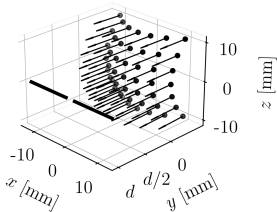
$$g = g(x, y, z, x') = \frac{\exp(-jkR)}{R},$$

$$R = |(x'), (x, y, z)|$$

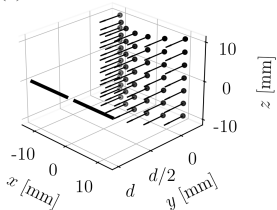
- A center-fed half-wavelength dipole, the input power normalized to 10 mW
- Current distribution, $I(x')$, governed by the Pocklington integro-differential equation →
(a) GB-IBEM, (b) GB-IBEM + neural network for smooth gradients at critical elements
- Electric-field components obtained at any point on the surface of the tissue → boundary element formalism with automatic differentiation
- Reference flat compared to (a) spherical and (b) cylindrical evaluation surfaces

Published paper #2: Model and methods

(a)



(b)



- A center-fed half-wavelength dipole, the input power normalized to 10 mW
- Current distribution, $I(x')$, governed by the Pocklington integro-differential equation → (a) GB-IBEM, (b) GB-IBEM + neural network for smooth gradients at critical elements
- Electric-field components obtained at any point on the surface of the tissue → boundary element formalism with automatic differentiation
- Reference flat compared to (a) spherical and (b) cylindrical evaluation surfaces

Published paper #2: Reported result and takeaways

- Time-averaged Poynting vector representing the direction and density of EM-power flow into the tissue

$$\mathbf{S} = \frac{1}{2} \Re (\mathbf{E} \times \mathbf{H}^*)$$

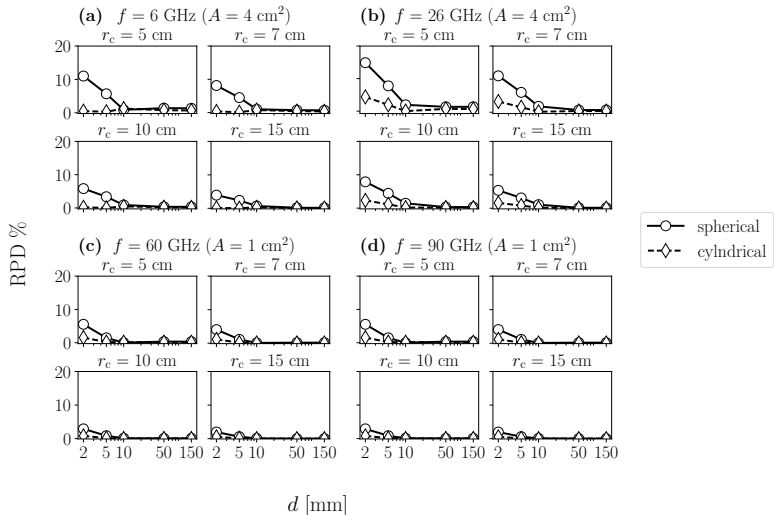
- Evaluation surface in cylindrical coordinate system (r, φ, z) , ISO 80000-2:2019

$$\mathbf{v}(\theta, \varphi) = [r \cos(\varphi), r \sin(\varphi), z]$$

- Definition: Normal component → cylindrical coordinate system

$$sPD_n = \frac{1}{A} \iint \mathbf{S}(\mathbf{v}) \cdot (\mathbf{v}_\varphi \times \mathbf{v}_z) \, d\varphi dz$$

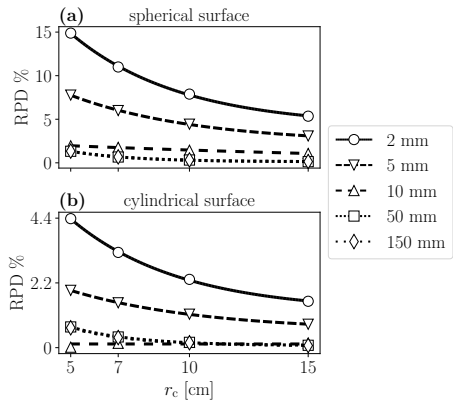
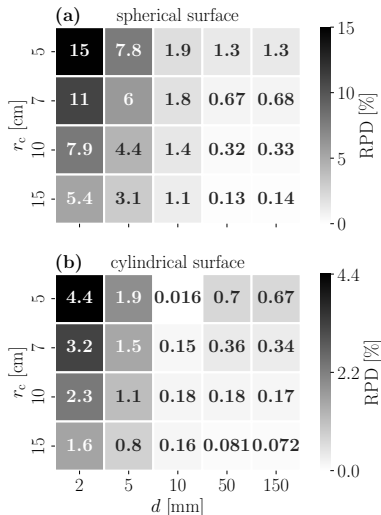
Published paper #2: Reported result and takeaways



Relative difference in sPD_n as a function of the separation distance between the spherical and flat, and between the cylindrical and flat evaluation surface for various curvature radii

Published paper #2: Reported result and takeaways

Relative difference in sPD_n at 26 GHz as a function of the separation distance parametrized by curvature radius: (a) flat-spherical, (b) flat-cylindrical



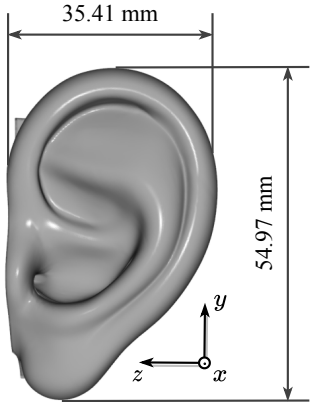
Published paper #3: Scope

Kapetanović, A., Sacco, G. et al. "Area-averaged transmitted and absorbed power density on a realistic ear model," in *IEEE J Electromagn RF Microw Med Biol*, 7(1):39–45, 2023, doi: 10.1109/JERM.2022.3225380

- Utilization of the anatomically detailed adult-human ear model⁴⁴
- Development of an accurate technique for power-density averaging on arbitrary surfaces
- Realization of the (first stage) automatic detection of peak spatial-average power density
- Validation of the approach by commercial EM-simulation packages
- Comparison of two existing definitions of the spatially averaged APD by considering volumetric and surface integral
- Comparison of dosimetric quantities extracted on the surface of the ear with the flat surface used as a reference

⁴⁴Sforza et al. 2009.

Published paper #3: Model and methods

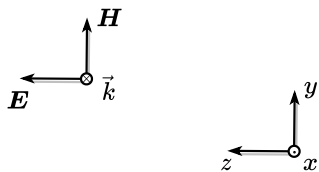


- Homogeneous adult-human ear model
 - complex permittivity of dry skin: $17.71 - j 16.87$ at 26 GHz and $7.98 - j 10.90$ at 60 GHz⁴⁵
 - Solution domain discretized by using the tetrahedral mesh (mesh cell length $\sim \lambda/8$) \rightarrow $\sim 15M$ mesh cells in total
 - finite element method (FEM)
- Exposure to the plane wave with two polarization modes
 - polarization 1 \rightarrow TE-like
 - polarization 2 \rightarrow TM-like

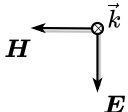
⁴⁵Gabriel 1996.

Published paper #3: Model and methods

TE-like polarization



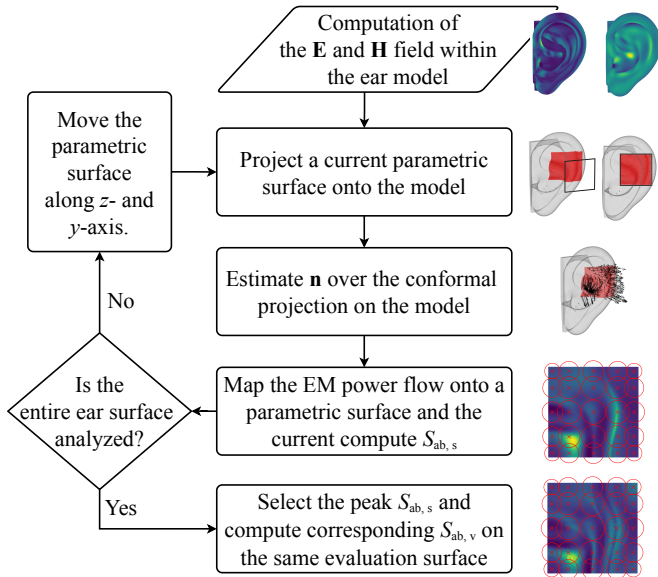
TM-like polarization



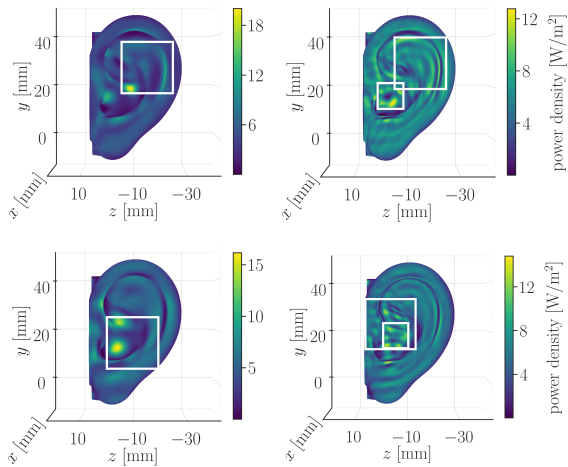
- Homogeneous adult-human ear model
 - complex permittivity of dry skin: $17.71 - j 16.87$ at 26 GHz and $7.98 - j 10.90$ at 60 GHz⁴⁵
 - Solution domain discretized by using the tetrahedral mesh (mesh cell length $\sim \lambda/8$) \rightarrow $\sim 15M$ mesh cells in total
 - finite element method (FEM)
- Exposure to the plane wave with two polarization modes
 - polarization 1 \rightarrow TE-like
 - polarization 2 \rightarrow TM-like

⁴⁵Gabriel 1996.

Published paper #3: Reported result and takeaways

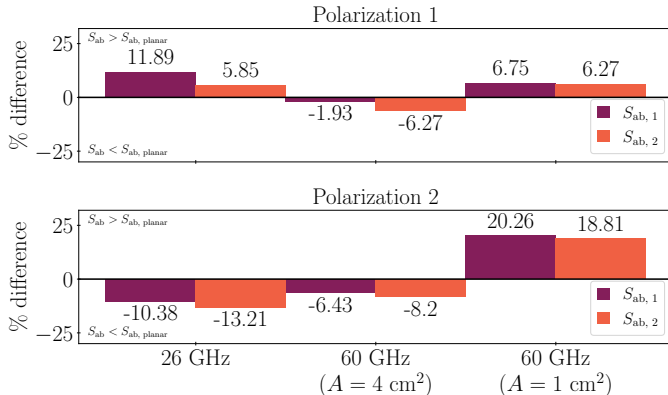


Published paper #3: Reported result and takeaways



"Hot-spot" regions; the top and bottom row correspond to TE- and TM-like polarization, respectively; the first and second column pertains to 26 and 60 GHz, respectively

Published paper #3: Reported result and takeaways



Relative differences between the two definitions of spatially averaged APD computed on the ear and planar homogeneous skin model

Published paper #4: Scope

Cvetković, M. et al. "On the applicability of numerical quadrature for double surface integrals at 5G frequencies," in *J Commun Softw Syst*, 18(1):42–53, 2022, doi: 10.24138/jcomss-2021-0183

- Investigation of the applicability of numerical integration to approximate surface integrals at 5G frequencies
- Realization of the comprehensive test suite for multiple combinations of the source and observation triangles
- Development of the unit-cube test
- Inspection of the effect of increasing frequency and discretization scheme on the convergence of numerical solution (herein the method of moments)

Published paper #3: Model and methods

$$\begin{aligned} & \sum_{n=1}^N \left(j\omega\mu_i A'_{mn,i} \frac{j}{\omega\epsilon_i} B_{mn,i} \right) J_n + \\ & + \sum_{n=1}^N (C_{mn,i} + D_{mn,i}) M_n \\ & = \begin{cases} V_m, & i = 1 \\ 0, & i = 2 \end{cases} \end{aligned}$$

- The numerical solution of the integral equation-based formulation results in the fully populated system matrix → size directly related to the frequency
- Numerical solution of the integral equation requires solving multiple double surface integrals
- Solution depends on the positional relationship between the surface elements (triangles) → unit-cube test

Published paper #3: Model and methods

$$A_{mn,i} = \int_S \mathbf{f}_m(\mathbf{r}) \cdot \\ \cdot \int_{S'} \mathbf{f}_n(\mathbf{r}') G_i(\mathbf{r}, \mathbf{r}') dS' dS$$

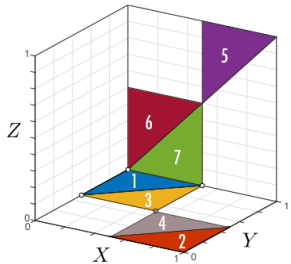
$$B_{mn,i} = \dots$$

$$C_{mn,i} = \dots$$

$$D_{mn,i} = \dots$$

- The numerical solution of the integral equation-based formulation results in the fully populated system matrix → size directly related to the frequency
- Numerical solution of the integral equation requires solving multiple double surface integrals
- Solution depends on the positional relationship between the surface elements (triangles) → unit-cube test

Published paper #3: Model and methods



- The numerical solution of the integral equation-based formulation results in the fully populated system matrix → size directly related to the frequency
- Numerical solution of the integral equation requires solving multiple double surface integrals
- Solution depends on the positional relationship between the surface elements (triangles) → unit-cube test

Published paper #3: Reported result and takeaways

- Numerical solution at high-gigahertz frequencies (e.g., at 90 GHz) → high quadrature order + “good enough” discretization scheme → increased demand for matrix storage and fill-time
- Optimal quadrature technique → low computational demand without sacrificing accuracy of the solution
- Reported convergence test → automatic selection of the suitable (fine balance between accuracy and efficiency) integration order

Table of contents

1. Introduction
2. Materials and methods
3. Application of research results
4. Concluding remarks

Concluding remarks

- more realistic (nonplanar canonical or anatomical) models of human body parts exposed to RF EM fields above 6 GHz, replacing previous flat models
- the accurate numerical technique for efficiently evaluating the scalar and vector field surface integrals
- the computationally efficient algorithm for automatic detection of “hot-spots” regions is developed for proposed models
- extensive dosimetric analysis of absorbed and incident EM power density using rigorous mathematical definitions and without simplification of the evaluation surface morphology

Questions and answers

Thank you!

References I

-  Anderson, Vitas, Rodney Croft, and Robert L. McIntosh (2010). "SAR versus S_{inc} : What is the appropriate RF exposure metric in the range 1–10 GHz? Part I: Using planar body models". In: *Bioelectromagnetics* 31.6, pp. 454–466. DOI: 10.1002/bem.20578.
-  Andrews, Jeffrey G. et al. (2014). "What will 5G be?" In: *IEEE Journal on Selected Areas in Communications* 32.6, pp. 1065–1082. DOI: 10.1109/JSAC.2014.2328098.
-  Ben-Shabat, Y. and Stephen Gould (2020). "DeepFit: 3D surface fitting via neural network weighted least squares". In: *In proceedings of the 2020 European Conference on Computer Vision*. Glasgow, UK, pp. 20–34. DOI: 10.1007/978-3-030-58452-8_2.
-  Ben-Shabat, Y., M. Lindenbaum, and A. Fischer (2019). "Nesti-Net: Normal estimation for unstructured 3D point clouds Using convolutional neural networks". In: *In proceedings of the 2019 IEEE/CVF Conference on Computer Vision and Pattern Recognition (CVPR)*. Long Beach, CA, USA, pp. 10104–10112. DOI: 10.1109/CVPR.2019.01035.

References II

-  Bentley, Jon Louis (1975). "Multidimensional binary search trees used for associative searching". In: *Communications of the Association for Computing Machinery* 18.9, pp. 509–517. DOI: [10.1145/361002.361007](https://doi.org/10.1145/361002.361007).
-  Carrasco, Eduardo et al. (2019). "Exposure assessment of portable wireless devices above 6 GHz". In: *Radiation Protection Dosimetry* 183.4, pp. 489–496. DOI: [10.1093/rpd/ncy177](https://doi.org/10.1093/rpd/ncy177).
-  Cazals, F. and M. Pouget (2005). "Estimating differential quantities using polynomial fitting of osculating jets". In: *Computer Aided Geometric Design* 22.2, pp. 121–146. DOI: [10.1016/j.cagd.2004.09.004](https://doi.org/10.1016/j.cagd.2004.09.004).
-  Charles, R. Q. et al. (2017). "PointNet: Deep learning on point sets for 3D classification and segmentation". In: *In proceedings of the 2017 IEEE Conference on Computer Vision and Pattern Recognition (CVPR)*. Honolulu, Hawaii, pp. 77–85. DOI: [10.1109/CVPR.2017.16](https://doi.org/10.1109/CVPR.2017.16).
-  Colombi, D., B. Thors, and C. Törnevik (2015). "Implications of EMF Exposure Limits on Output Power Levels for 5G Devices Above 6 GHz". In: *IEEE Antennas and Wireless Propagation Letters* 14, pp. 1247–1249. DOI: [10.1109/LAWP.2015.2400331](https://doi.org/10.1109/LAWP.2015.2400331).

References III

-  De Santis, Valerio et al. (2022). "On the Correlation Between Incident Power Density and Temperature Increase for Exposures at Frequencies Above 6 GHz". In: *IEEE Access* 10, pp. 82236–82245. DOI: [10.1109/ACCESS.2022.3195887](https://doi.org/10.1109/ACCESS.2022.3195887).
-  Diao, Yinliang, Kun Li, et al. (2021). "Effect of incidence angle on the spatial-average of incident power density definition to correlate skin temperature rise for millimeter wave exposures". In: *IEEE Transactions on Electromagnetic Compatibility* 63.5, pp. 1709–1716. DOI: [10.1109/TEMC.2021.3098594](https://doi.org/10.1109/TEMC.2021.3098594).
-  Diao, Yinliang, Essam A Rashed, and Akimasa Hirata (2020). "Assessment of absorbed power density and temperature rise for nonplanar body model under electromagnetic exposure above 6 GHz". In: *Physics in Medicine & Biology* 65. DOI: [10.1088/1361-6560/abbdb7](https://doi.org/10.1088/1361-6560/abbdb7).
-  Foster, K. R., M. C. Ziskin, and Q. Balzano (2016). "Thermal response of human skin to microwave energy: A critical review". In: *Health Physics* 111.6, pp. 528–541. DOI: [10.1097/HP.0000000000000571](https://doi.org/10.1097/HP.0000000000000571).
-  — (2017). "Thermal modeling for the next generation of radio-frequency exposure limits: Commentary". In: *Health Physics* 113.1, pp. 41–53. DOI: [10.1097/HP.0000000000000671](https://doi.org/10.1097/HP.0000000000000671).

References IV

-  Foster, K. R., M. C. Ziskin, Q. Balzano, and G. Bit-Babik (2018). "Modeling Tissue Heating From Exposure to Radio-frequency Energy and Relevance of Tissue Heating to Exposure Limits: Heating Factor". In: *Health Physics* 115.2, pp. 295–307. DOI: [10.1097/HP.0000000000000854](https://doi.org/10.1097/HP.0000000000000854).
-  Funahashi, Daisuke, Akimasa Hirata, et al. (2018). "Area-Averaged Transmitted Power Density at Skin Surface as Metric to Estimate Surface Temperature Elevation". In: *IEEE Access* 6, pp. 77665–77674. DOI: [10.1109/ACCESS.2018.2883733](https://doi.org/10.1109/ACCESS.2018.2883733).
-  Funahashi, Daisuke, Takahiro Ito, et al. (2018). "Averaging Area of Incident Power Density for Human Exposure from Patch Antenna Arrays". In: *IEICE Transactions on Electronics* E101.C.8, pp. 644–646. DOI: [10.1587/transele.E101.C.644](https://doi.org/10.1587/transele.E101.C.644).
-  Gabriel, Camelia (1996). "Compilation of the Dielectric Properties of Body Tissues at RF and Microwave Frequencies". In: *US Air Force*. Vol. Final Technical Report, TR-1996-0037. DOI: [10.21236/ada303903](https://doi.org/10.21236/ada303903).
-  Guerrero, P. et al. (2018). "PCPNet: Learning local shape properties from raw point clouds". In: *Computer Graphics Forum* 37.2, pp. 75–85. DOI: [10.1111/cgf.13343](https://doi.org/10.1111/cgf.13343).

References V

-  Hashimoto, Y. et al. (2017). "On the averaging area for incident power density for human exposure limits at frequencies over 6 GHz". In: *Physics in Medicine & Biology* 62.8, pp. 3124–3138. DOI: [10.1088/1361-6560/aa5f21](https://doi.org/10.1088/1361-6560/aa5f21).
-  He, Wang et al. (2018). "RF compliance study of temperature elevation in human head model around 28 GHz for 5G user equipment application: Simulation analysis". In: *IEEE Access* 6, pp. 830–838. DOI: [10.1109/ACCESS.2017.2776145](https://doi.org/10.1109/ACCESS.2017.2776145).
-  Huang, Hui et al. (2009). "Consolidation of unorganized point clouds for surface reconstruction". In: *ACM Transactions on Graphics* 28.5, pp. 1–7. DOI: [10.1145/1618452.1618522](https://doi.org/10.1145/1618452.1618522).
-  IEEE International Committee on Electromagnetic Safety (ICES) Technical Committee (TC) 95 (2019). "Standard for safety levels with respect to human exposure to electric, magnetic, and electromagnetic fields, 0 Hz to 300 GHz". In: *IEEE Std C95.1-2019 (Revision of IEEE Std C95.1-2005/ Incorporates IEEE Std C95.1-2019/Cor 1-2019)*, pp. 1–312. DOI: [10.1109/IEEESTD.2019.8859679](https://doi.org/10.1109/IEEESTD.2019.8859679).
-  — (2021). "Guide for the definition of incident power density to correlate surface temperature elevation". In: *IEEE Std 2889-2021*, pp. 1–152. DOI: [10.1109/IEEESTD.2021.9650810](https://doi.org/10.1109/IEEESTD.2021.9650810).

References VI

-  Innes, Mike et al. (2019). *A differentiable programming system to bridge machine learning and scientific computing*. arXiv: 1907.07587 [cs.PL].
-  International Commission on Non-Ionizing Radiation Protection (ICNIRP) (2020a). “Guidelines for limiting exposure to electromagnetic fields (100 kHz to 300 GHz)”. In: *Health Physics* 118, pp. 483–524. DOI: 10.1097/HP.0000000000001210.
-  — (2020b). “Principles for Non-Ionizing Radiation Protection”. In: *Health Physics* 118.5, pp. 477–482. DOI: 10.1097/HP.0000000000001252.
-  Kapetanovic, Ante and Dragan Poljak (2021). “Application of automatic differentiation in electromagnetic dosimetry: Assessment of the absorbed power density in the mmWave frequency spectrum”. In: *In proceedings of the 2021 International Conference on Smart and Sustainable Technologies*. Split, Croatia. DOI: 10.23919/SpliTech52315.2021.9566429.
-  Kapetanović, Ante and Dragan Poljak (2022). “Assessment of incident power density on spherical head model up to 100 GHz”. In: *IEEE Transactions on Electromagnetic Compatibility* 64.5, pp. 1296–1303. DOI: 10.1109/TEMC.2022.3183071.

References VII

-  Kapetanović, Ante and Dragan Poljak (2023). "Machine learning-assisted antenna modelling for realistic assessment of incident power density on non-planar surfaces above 6 GHz". In: *Radiation Protection Dosimetry* 199.8–9, pp. 826–834. DOI: 10.1093/rpd/ncad114.
-  Kapetanović, Ante, Dragan Poljak, and Hrvoje Dodig (2023). "Automatic detection of peak spatial-average power density on nonplanar body models". In: *In proceedings of the 31st International Conference on Software, Telecommunications and Computer Networks*. Split Croatia.
-  Kapetanović, Ante, Giulia Sacco, et al. (2023). "Area-averaged transmitted and absorbed power density on a realistic ear model". In: *IEEE Journal of Electromagnetics, RF and Microwaves in Medicine and Biology* 7.1, pp. 39–45. DOI: 10.1109/JERM.2022.3225380.
-  Katz, S., A. Tal, and R. Basri (2007). "Direct visibility of point sets". In: *ACM Transactions on Graphics* 26.3, pp. 24–35. DOI: 10.1145/1276377.1276407.
-  Kazhdan, Michael, Matthew Bolitho, and Hugues Hoppe (2006). "Poisson surface reconstruction". In: *In proceedings of the 2006 Eurographics Symposium on Geometry Processing*. Cagliari, Sardinia, Italy, pp. 61–70.

References VIII

-  Kushiyama, Yujiro and Tomoaki Nagaoka (2022). “Absorbed power density on a spherical model exposed to electromagnetic field from phased array antennas”. In: *2022 Asia-Pacific Microwave Conference (APMC)*, pp. 961–963. DOI: [10.23919/APMC55665.2022.9999896](https://doi.org/10.23919/APMC55665.2022.9999896).
-  Laakso, I. et al. (2015). “Inter-subject variability in electric fields of motor cortical tDCS”. In: *Brain Stimulation* 8.5, pp. 906–913. DOI: [10.1016/j.brs.2015.05.002](https://doi.org/10.1016/j.brs.2015.05.002).
-  Lenssen, J. E., C. Osendorfer, and J. Masci (2020). “Deep iterative surface normal estimation”. In: *In proceedings of the 2020 IEEE/CVF Conference on Computer Vision and Pattern Recognition (CVPR)*. Virtual, pp. 11244–11253. DOI: [10.1109/CVPR42600.2020.01126](https://doi.org/10.1109/CVPR42600.2020.01126).
-  Levin, D. (1998). “The approximation power of moving least-squares”. In: *Mathematics of Computation* 67, pp. 1517–1531. DOI: [10.1090/S0025-5718-98-00974-0](https://doi.org/10.1090/S0025-5718-98-00974-0).
-  Li, Chung-Huan et al. (2012). “Mechanisms of RF electromagnetic field absorption in human hands and fingers”. In: *IEEE Transactions on Microwave Theory and Techniques* 60.7, pp. 2267–2276. DOI: [10.1109/TMTT.2012.2197019](https://doi.org/10.1109/TMTT.2012.2197019).

References IX

-  Li, Kun, Sachiko Kodera, et al. (2023). "Calculated epithelial/absorbed power density for exposure from antennas at 10–90 GHz: Intercomparison study using a planar skin model". In: *IEEE Access* 11, pp. 7420–7435. DOI: [10.1109/ACCESS.2023.3238582](https://doi.org/10.1109/ACCESS.2023.3238582).
-  Li, Kun, Kensuke Sasaki, Kanako Wake, et al. (2021). "Quantitative Comparison of Power Densities Related to Electromagnetic Near-Field Exposures With Safety Guidelines From 6 to 100 GHz". In: *IEEE Access* 9, pp. 115801–115812. DOI: [10.1109/ACCESS.2021.3105608](https://doi.org/10.1109/ACCESS.2021.3105608).
-  Li, Kun, Kensuke Sasaki, Soichi Watanabe, et al. (2019). "Relationship between power density and surface temperature elevation for human skin exposure to electromagnetic waves with oblique incidence angle from 6 GHz to 1 THz". In: *Physics in Medicine & Biology* 64.6, p. 065016. DOI: [10.1088/1361-6560/ab057a](https://doi.org/10.1088/1361-6560/ab057a).
-  McIntosh, Robert L. and Vitas Anderson (2010). "SAR versus S_{inc} : What is the appropriate RF exposure metric in the range 1–10 GHz? Part II: Using complex human body models". In: *Bioelectromagnetics* 31.6, pp. 467–478. DOI: [10.100/bem.20574](https://doi.org/10.100/bem.20574).

References X

-  Miura, Norika et al. (2021). "Power Absorption and Skin Temperature Rise From Simultaneous Near-Field Exposure at 2 and 28 GHz". In: *IEEE Access* 9, pp. 152140–152149. DOI: [10.1109/ACCESS.2021.3126372](https://doi.org/10.1109/ACCESS.2021.3126372).
-  Mohammad Rouhani Angel D. Sappa, Edmond Boyer (2015). "Implicit B-spline surface reconstruction". In: *IEEE Transactions on Image Processing* 24.1, pp. 22–32. DOI: [10.1109/TIP.2014.2366374](https://doi.org/10.1109/TIP.2014.2366374).
-  Morimoto, Ryota and Akimasa Hirata (2022). "Assessment of incident power density in different shapes of averaging area for radio-frequency exposure above 6 GHz". In: *Physics in Medicine & Biology* 67.21, p. 215014. DOI: [10.1088/1361-6560/ac994d](https://doi.org/10.1088/1361-6560/ac994d).
-  Nakae, Takuma et al. (2020). "Skin Temperature Elevation for Incident Power Densities From Dipole Arrays at 28 GHz". In: *IEEE Access* 8, pp. 26863–26871. DOI: [10.1109/ACCESS.2020.2970219](https://doi.org/10.1109/ACCESS.2020.2970219).
-  Poljak, Dragan (2007). *Advanced Modeling in Computational Electromagnetic Compatibility*. John Wiley & Sons, Inc., New Jersey, US. ISBN: 978-0-470-03665-5.

References XI

-  Rappaport, Theodore S. et al. (2013). "Millimeter wave mobile communications for 5G cellular: It will work!" In: *IEEE Access* 1, pp. 335–349. DOI: 10.1109/ACCESS.2013.2260813.
-  Sacco, Giulia, Zain Haider, and Maxim Zhadobov (2022). "Exposure levels induced in curved body parts at mmWaves". In: *IEEE Journal of Electromagnetics, RF and Microwaves in Medicine and Biology* 6.3, pp. 413–419. DOI: 10.1109/JERM.2022.3178604.
-  Sasaki, Kensuke et al. (2017). "Monte Carlo simulations of skin exposure to electromagnetic field from 10 GHz to 1 THz". In: *Physics in Medicine & Biology* 62 (17), pp. 6993–7010. DOI: 10.1088/1361-6560/aa81fc.
-  Sforza, Chiarella et al. (2009). "Age- and sex-related changes in the normal human ear". In: *Forensic Science International* 187.1, 110.e1–110.e7. ISSN: 0379-0738. DOI: j.forsciint.2009.02.019.
-  Taguchi, Kenji et al. (2022). "Computation of Absorbed Power Densities in High-Resolution Head Models by Considering Skin Thickness in Quasi-Millimeter and Millimeter Wave Bands". In: *IEEE Journal of Electromagnetics, RF and Microwaves in Medicine and Biology* 6.4, pp. 516–523. DOI: 10.1109/JERM.2022.3203576.

References XII

-  Thors, Björn et al. (2016). "Exposure to RF EMF From Array Antennas in 5G Mobile Communication Equipment". In: *IEEE Access* 4, pp. 7469–7478. DOI: 10.1109/ACCESS.2016.2601145.
-  World Health Organization (WHO) (n.d.). *Constitution of the World Health Organization – Preamble*.
<https://www.who.int/about/governance/constitution>. accessed on May 23rd 2023. URL:
<https://www.who.int/about/governance/constitution>.
-  Wu, Ting, Theodore S. Rappaport, and Christopher M. Collins (2015). "Safe for generations to come: Considerations of safety for millimeter waves in wireless communications". In: *IEEE Microwave Magazine* 16.2, pp. 65–84. DOI: 10.1109/MMM.2014.2377587.
-  Xu, Bo et al. (2017). "Understandings of maximum spatially-averaged power density in 5G RF EMF exposure study". In: *In proceedings of the 2017 International Workshop on Antenna Technology: Small Antennas, Innovative Structures, and Applications (iWAT)*. Athens, Greece, pp. 115–117. DOI: 10.1109/IWAT.2017.7915332.

References XIII

-  Zhadobov, Maxim et al. (2011). "Millimeter-wave interactions with the human body: State of knowledge and recent advances". In: *International Journal of Microwave and Wireless Technologies* 3.2, pp. 237–247. DOI: [10.1017/S1759078711000122](https://doi.org/10.1017/S1759078711000122).
-  Zhu, R. et al. (2021). "AdaFit: Rethinking learning-based normal estimation on point clouds". In: *In proceedings of the 2021 IEEE/CVF International Conference on Computer Vision (ICCV)*. Montreal, QC, Canada, pp. 6098–6107. DOI: [10.1109/ICCV48922.2021.00606](https://doi.org/10.1109/ICCV48922.2021.00606).
-  Ziskin, M. C. et al. (2018). "Tissue models for RF exposure evaluation at frequencies above 6 GHz". In: *Bioelectromagnetics* 39.3, pp. 173–189. DOI: [10.1002/bem.22110](https://doi.org/10.1002/bem.22110).